Check for updates

Ruthenium-based electrocatalyst for efficient acidic water oxidation in PEM water electrolysis for H$_2$ production

Yinan Tao,[a] Ruilin Zhang,[c] Junyan Chen,[a] Wubin Weng,[ab] Yong He[ab] and Zhihua Wang [ID] *[ab]

Proton exchange membrane (PEM) water electrolysis is a promising and sustainable technology for hydrogen production. Currently, the anode catalysts used in PEM water electrolysis are predominantly iridium-based electrocatalysts, which are extremely precious and scarce. In this study, we report a mixed (Ru–W)O$_x$ catalyst as a promising alternative to iridium-based catalysts. The (Ru–W)O$_x$ catalyst was synthesized using a simple Pechini–Adams method, and its microstructure and electrochemical performance were optimized by controlling the Ru/W doping ratio and the synthesis temperature. Among the synthesized catalysts, the Ru$_6$W$_4$O$_x$ catalyst prepared at 400 °C demonstrated the best oxygen evolution reaction (OER) activity and stability, achieving an overpotential of only 140.32 mV at 10 mA cm^{-2}. Furthermore, after a 150 hours stability test, no significant loss in catalytic activity was observed. When applied to the anode of a PEM water electrolyzer, the Ru$_6$W$_4$O$_x$-400 °C catalyst exhibited an impressively low cell voltage of 1.784 V at 2 A cm^{-2}. The energy consumption is as low as 4.34 kWh m^{-3} H$_2$. These results provide new insights for developing efficient and stable non-iridium-based OER catalysts for PEM water electrolysis.
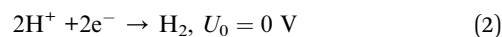
1 Introduction

Hydrogen is considered a crucial element for achieving deep decarbonization of modern energy systems. Water electrolysis powered by renewable electricity offers a "zero-carbon" pathway for hydrogen production. With the large-scale expansion and cost reduction of renewable energy, the green hydrogen production pathway has become highly promising. Among various water electrolysis technologies, proton exchange membrane (PEM) electrolysis stands out due to its fast dynamic response, wide operating load range, and compact system structure.[1–4] These features make PEM electrolysis suitable for coupling with intermittent renewable energy sources to produce green hydrogen.

PEM electrolysis technology uses a sulfonated polymer membrane as the electrolyte, with hydrogen ions(H$^+$) as the ionic carriers. Deionized water permeates through the proton-conducting membrane, enabling electrochemical reactions that consist of two half-cell processes:[5]

Anode – Oxygen Evolution Reaction (OER):

$$H_2O \rightarrow 2H^+ + 1/2O_2 + 2e^-, \ U_0 = 1.23 \text{ V} \qquad (1)$$
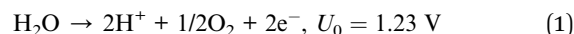
Cathode – Hydrogen Evolution Reaction (HER):

$$2H^+ + 2e^- \rightarrow H_2, \ U_0 = 0 \text{ V} \qquad (2)$$

At the anode, water is split into oxygen molecules, protons, and electrons. This process imposes harsh working conditions on the components of PEM electrolyzers, including high potential, oxidative stress, and severe corrosiveness.[6] These stringent conditions significantly limit the choice of materials. Currently, OER catalysts suitable for PEM systems still rely on the extremely scarce and expensive precious metal iridium (Ir) and its oxides. Consequently, extensive research efforts have been devoted to developing electrocatalysts with reduced Ir content while achieving higher activity and stability.[7–10] Strategies include doping with non-precious metals, incorporating support materials, and tailoring catalyst morphologies.[11–13]

Compared to Ir, ruthenium (Ru) is the most active metal for acidic OER due to its optimal binding energy with oxygen-related intermediates.[14] Additionally, Ru is more abundant in Earth's crust and significantly less expensive than Ir (Ir ≈ US$140/g, Ru ≈ US$16/g).[15] However, the stability of Ru-based catalysts remains a critical challenge, as Ru is prone to excessive oxidation under acidic conditions. This leads to lattice oxygen loss, structural instability, and accelerated catalyst degradation. Thus, while Ru exhibits excellent OER activity,

[a]State Key Laboratory of Clean Energy Utilization, Zhejiang University, Hangzhou 310027, P. R. China. E-mail: wangzh@zju.edu.cn

[b]Qingshanhu Energy Research Center, Zhejiang University, Hangzhou, 311300, P. R. China

[c]Hoymiles Power Electronics Inc., Hangzhou, 310015, P. R. China

improving its structural stability during prolonged operation remains a key hurdle.

In recent years, researchers have focused on using metal doping strategies to enhance the performance of Ru-based catalysts.[15–30] High-entropy or multi-metal oxides based on Ru can form strong metal–oxygen (M–O) bonds, suppressing lattice oxygen over-oxidation.[8] For example, Su *et al.* synthesized Cu-doped hollow porous RuO_2 polyhedral structures using a Cu-BTC precursor. The Cu-doped RuO_2 exhibited excellent OER performance, achieving a current density of 10 mA cm^{-2} with a low overpotential of 188 mV in 0.5 M H_2SO_4. It also demonstrated high stability over 10 000 CV cycles and 8 hours of chronoamperometric testing. The enhanced performance was attributed to the highly unsaturated Ru sites on high-index facets and the electronic structure modulation induced by Cu doping.[30] Chen *et al.* reported Mn-doped RuO_2, achieving an overpotential as low as 158 mV at 10 mA cm^{-2} in 0.5 M H_2SO_4, with moderate stability. DFT calculations indicated that Mn doping regulated the d-band center of Ru sites, enhancing intrinsic activity.[22]

Studies on Ru and Tungsten (W) co-doped oxides are also emerging. Wang *et al.* synthesized the heterogeneous catalyst W-IrRu$_3$O$_x$. The W-IrRu$_3$O$_x$ catalyst exhibits high corrosion resistance, along with a low overpotential of 249 mV at 10 mA m^{-2} and a low Tafel slope of 64 mV dec^{-1}. During the chronoamperometric test, η_{10} of W-IrRu$_3$O$_x$ increases from 231 to ∼300 mV in the first ∼30 h and then remains nearly unchanged during the subsequent period.[21] However, challenges remain, including complex synthesis methods, high precious metal content, and limited testing under high current densities in practical electrolyzers.

In this study, a series of $(Ru–W)O_x$ catalysts were synthesized using a simple two-step method. By systematically adjusting doping ratios and calcination temperatures, a comprehensive evaluation was conducted for the developed catalysts' performance in OER, including activity, reaction kinetics, and long-term stability. The results will provide important insights into optimizing Ru-based catalysts and preparation parameters, offering new strategies for designing efficient and stable OER catalysts under acidic conditions.

2 Experimental methods

2.1 Synthesis of catalysts

The $(Ru–W)O_x$ catalysts were synthesized using the Pechini–Adams method. By controlling the precursor ratios and calcination temperatures, nanoscale catalysts with smaller particle sizes and desirable morphologies were obtained, which enhanced the electrochemically active surface area and improved reaction efficiency.[31] $RuCl_3 \cdot 3H_2O$ and WCl_6 with varying molar ratios were dissolved in ultrapure water under vigorous stirring and ultrasonicated for 30 minutes. Separately, 150 mg of EDTA and 60 mg of citric acid were dissolved in ultrapure water and gradually added to the $RuCl_3 \cdot 3H_2O$ and WCl_6 solution. The mixture was then stirred continuously at room temperature for 4 hours to ensure uniform dispersion of the components.

Subsequently, the mixture was heated in a water bath at 90 °C while stirring until the solution completely evaporated. The dried catalyst was transferred to a ceramic crucible and calcined in a muffle furnace at a temperature of 400 °C for 2 hours, with a ramp rate of 5 °C min^{-1}. After being annealed, the samples were allowed to cool naturally to room temperature, followed by multiple rounds of high-speed centrifugation using 10 wt% $HClO_4$ solution, ultrapure water, and ethanol to wash the catalyst. The supernatant was discarded after each wash. Finally, the sediment was dried in an oven at 80 °C, collected, and stored in sealed sample vials under controlled temperature and humidity.

The catalysts were labeled based on the molar ratios of Ru to W in the precursors as $Ru_9W_1O_x$-400 °C, $Ru_8W_2O_x$-400 °C, $Ru_7W_3O_x$-400 °C, $Ru_6W_4O_x$-400 °C, $Ru_5W_5O_x$-400 °C, and $Ru_4W_6O_x$-400 °C. Additionally, a single-metal Ru-based oxide catalyst was prepared using a similar method and labeled as RuO_x-400 °C.

2.2 Characterization of catalysts

The surface morphology and microstructure of the $(Ru–W)O_x$ catalysts were characterized using a transmission electron microscope (TEM, FEI Tecnai G2 F20 S-TWIN and FEI Tecnai G2 F20 S-TWIN) equipped with energy-dispersive X-ray spectroscopy (EDX) to analyze elemental distribution on the surface. X-ray diffraction (XRD, X-pert Powder) was employed to determine the structural and crystalline properties of the catalysts, with a scan range of $2\theta = 20-80°$. X-ray photoelectron spectroscopy (XPS, Thermo Scientific K-Alpha) was used to analyze the surface elemental composition and oxidation states of the catalysts.

2.3 Electrochemical Measurements

The electrochemical performance of the synthesized $(Ru–W)O_x$ catalysts and commercial RuO_2 catalyst (hereafter referred to as COM-RuO_2, purchased from Shanghai Macklin Co., Ltd) was evaluated using a standard three-electrode electrochemical cell system. The experimental setup included an electrochemical workstation (AUTOLAB PGSTAT302N) and a 100 mL cylindrical glass electrolysis cell. The three-electrode system comprised a 3 mm diameter glassy carbon electrode (working electrode), a 0.5 mm × 37 mm platinum wire (counter electrode), and a $HgSO_4$ reference electrode (reference potential of 0.65 V *vs.* RHE). The electrolyte was 0.5 M H_2SO_4 solution. For consistency, all potentials were converted to values *versus* reversible hydrogen electrodes according to $E(RHE) = E(WE) + 0.65 + 0.0592$ pH.

The catalyst ink was prepared by mixing 2 mg of $(Ru–W)O_x$ or COM-RuO_2 catalyst, 20 μL of 5 wt% Nafion solution, and 285 μL of isopropanol. The mixture was ultrasonicated for more than 30 minutes at temperatures below 25 °C. A micropipette was used to deposit 1 μL of the ink onto the black surface of the glassy carbon electrode, allowing each layer to dry completely before adding the next. A total of 5 μL of ink was applied.

Linear sweep voltammetry (LSV) was performed to obtain the polarization curves and corresponding overpotential values, with the potential range set from 1.3 to 1.8 V and a scan rate of 10 mV s^{-1}. Electrochemical impedance spectroscopy (EIS) was used to measure the impedance of the catalyst under different frequencies, applying a sinusoidal perturbation of 10 mV at 1.45 V *vs.* RHE, with a frequency range of 10 kHz to 10 mHz. The

cost-effectiveness of the catalyst was evaluated by calculating the mass activity(normalized by Ru). The Ru mass fraction in the catalyst was determined based on EDX results obtained from TEM characterization.

Cyclic voltammetry (CV) was performed to determine the double-layer capacitance (C_{dl}), revealing the electrochemical surface area (ECSA). Scans were conducted within the non-faradaic range of 0.82–0.92 V at scan rates of 20, 40, 60, 80, and 100 mV s^{-1}. The ECSA was evaluated from the C_{dl} according to ECSA = $C_{dl}/C_s m_{loading}$. C_s is the sample's specific capacitance or the capacitance of an atomically smooth planar surface of the material per unit under identical electrolyte conditions, and is usually assumed as 0.035 mF cm^{-2} in H$_2$SO$_4$ electrolyte; $m_{loading}$ is the mass of the load catalyst. Chronoamperometry (CA) was used to assess the long-term electrochemical stability of the catalysts by applying a constant current density of 10 mA cm^{-2} to the electrode and recording the potential over a 24 hours period.

3 results and discussion

3.1 structures and morphologies of (Ru–W)O$_x$ electrocatalysts

The TEM images of catalysts with different Ru and W ratios and their corresponding selected area electron diffraction (SAED) patterns are shown in Fig. 1a–g. The images reveal a clear trend in crystallinity as the Ru content increases. As the Ru content increases and the W content decreases, the particle morphology gradually transitions from irregular amorphous structures to denser and more regular crystalline structures, with an increasing number of well-defined RuO$_2$ lattice fringes. Overall, W primarily appears in low-crystallinity or amorphous forms at this temperature, resulting in the presence of dispersed amorphous regions in the overall morphology. High-resolution TEM (HRTEM) analysis indicates well-defined lattice fringes with clear crystal surface spacing of about 3.2 Å (Fig. 1h), corresponding precisely to the (110) crystallographic plane of rutile RuO$_2$. This observation confirms the preservation of the host rutile structure in (Ru–W)O$_x$, consistent with the XRD results. Elemental mapping (Fig. 1i) demonstrates homogeneous spatial distribution of Ru, W, and O at nanoscale, indicating that W is uniformly doped in the RuO$_2$ matrix, rather than clustered in localized areas. The EDX analysis results, shown in Table 1, confirm that the Ru/W ratio in the synthesized catalysts is close to the initial feed ratio, indicating the successful synthesis of (Ru–W)O$_x$ catalysts. These results were subsequently used for the calculation of mass activity and ECSA.

The XRD patterns, shown in Fig. 2, show that all samples exhibit characteristic diffraction peaks corresponding to RuO$_2$ (JCPDS#43-1027), with three prominent peaks observed near 28°, 35°, and 54°, which can be attributed to the (110), (101),
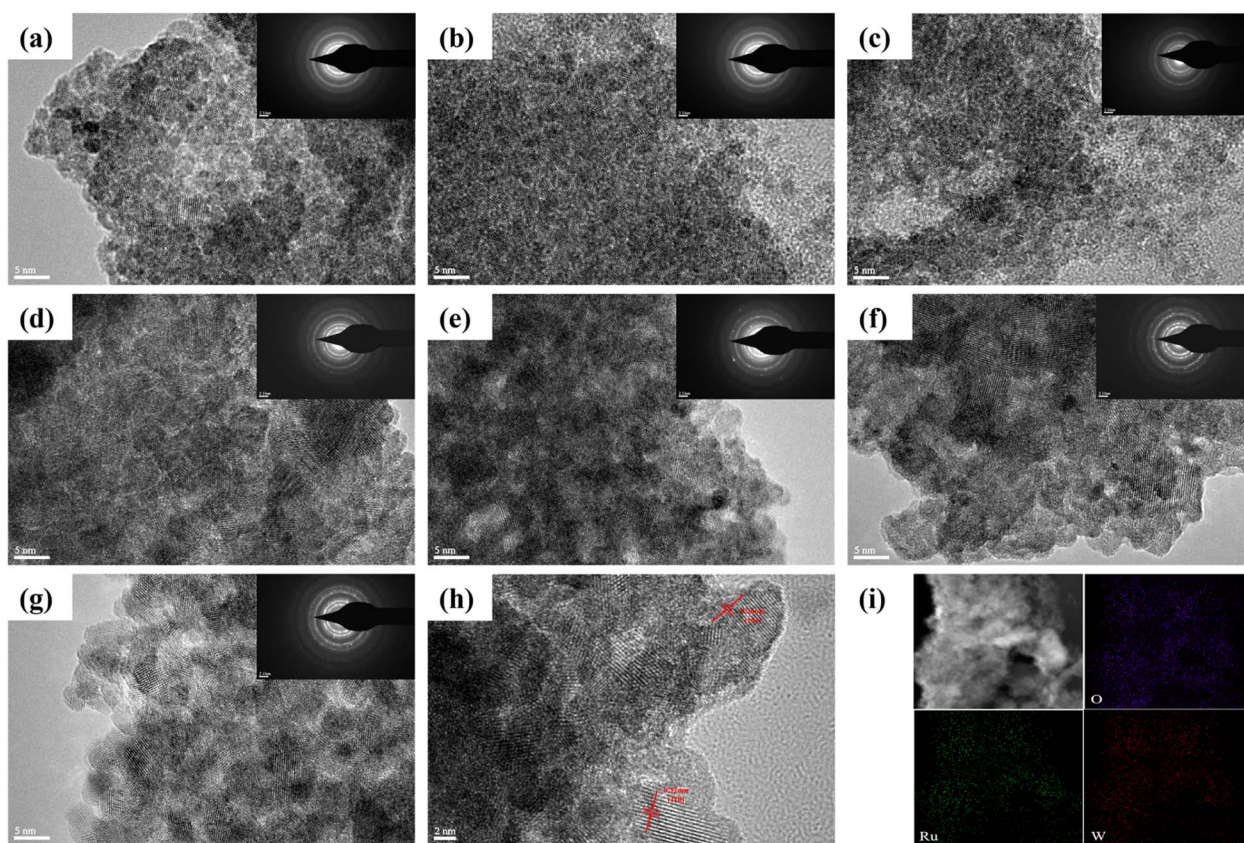

Fig. 1 TEM and SEAD images of (Ru–W)O$_x$ catalysts (a) Ru$_4$W$_6$O$_x$-400 °C, (b) Ru$_5$W$_5$O$_x$-400 °C, (c) Ru$_6$W$_4$O$_x$-400 °C, (d) Ru$_7$W$_3$O$_x$-400 °C, (e) Ru$_8$W$_2$O$_x$-400 °C, (f) Ru$_9$W$_1$O$_x$-400 °C, (g) RuO$_x$-400 °C, (h) marked HRTEM image of Ru$_6$W$_4$O$_x$-400 °C, (i) corresponding EDX elemental mapping of Ru$_6$W$_4$O$_x$-400 °C.

Table 1 Initial feeding and final element composition of (Ru−W)O$_x$ catalysts

Catalysts	Initial feeding			The synthesized catalysts			
	RuCl$_3$·3H$_2$O (mg)	WCl$_6$ (mg)	W/Ru (at%)	Ru (wt%)	W (wt%)	O (wt%)	W/Ru
RuO$_x$-400 °C	261.47	0	0	77.35	0	22.65	0
Ru$_9$W$_1$O$_x$-400 °C	235.32	39.66	0.11	72.67	15.85	11.48	0.12
Ru$_8$W$_2$O$_x$-400 °C	209.18	79.11	0.25	53.44	22.94	23.62	0.24
Ru$_7$W$_3$O$_x$-400 °C	183.03	118.97	0.43	42.51	35.26	22.23	0.45
Ru$_6$W$_4$O$_x$-400 °C	156.88	158.62	0.67	39.88	47.82	12.29	0.67
Ru$_5$W$_5$O$_x$-400 °C	130.74	198.28	1	30.22	51.61	18.17	0.93
Ru$_4$W$_6$O$_x$-400 °C	104.59	237.94	1.5	25.78	62.35	11.87	1.33
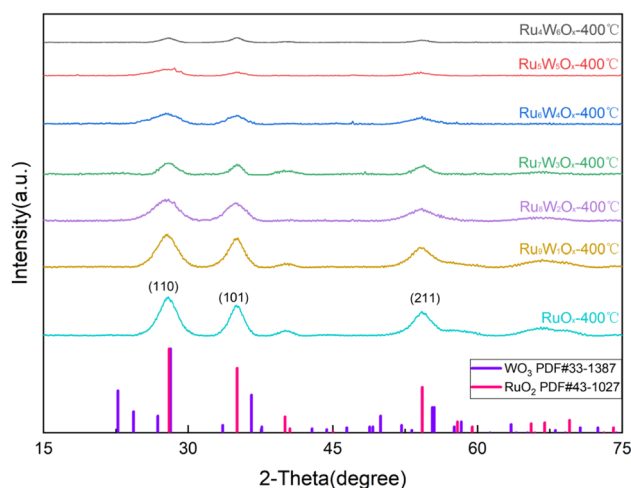
Fig. 2 XRD patterns of (Ru−W)O$_x$ catalysts.

and (211) planes of RuO$_2$, respectively. No distinct peaks corresponding to W oxides were observed, which is consistent with the TEM results. As the W doping ratio increases, the characteristic peaks of RuO$_2$ become less prominent, indicating that the addition of W affects the lattice structure of Ru oxides. At lower W doping levels, the diffraction peaks of RuO$_2$ remain sharp, while the peaks associated with WO$_3$ are relatively weak. This suggests that small amounts of W doping do not significantly disrupt the RuO$_2$ crystalline phase but may induce partial substitution or lattice distortion without forming a separate WO$_3$ phase. Furthermore, with increasing W content, the characteristic peaks near 28°, 35°, and 54° gradually shift slightly toward higher angles. This shift indicates lattice expansion, which can be attributed to the difference in ionic radii between Ru^{4+} (0.62 Å) and W^{4+} (0.66 Å).

Surface chemical states of the catalysts were systematically studied through XPS. The XPS full spectra confirm the presence of W in (Ru−W)O$_x$, consistent with the elemental mapping results. Since C 1s and Ru 3d spectra overlap, the secondary intense peak of Ru (Ru 3p) was measured for further contrast. The Ru 3p spectra (Fig. 3 and Table 2) could be deconvoluted into two pairs of peaks. The peaks at binding energies of 484–487 (Ru 3p$_{1/2}$) and 461–464 eV (Ru 3p$_{3/2}$) could be attributed to Ru^{4+} and low-valence Ru species. Additional peaks at higher binding energies (463.7–464.7 eV for Ru 3p$_{3/2}$ and 485.6–486.8 eV for Ru 3p$_{1/2}$) corresponded to satellite peaks of Ru. Compared with RuO$_x$, the Ru 3p peaks of (Ru−W)O$_x$ were shifted to a lower binding energy. Generally, a decrease in binding energy suggests an increase in electronic density, potentially
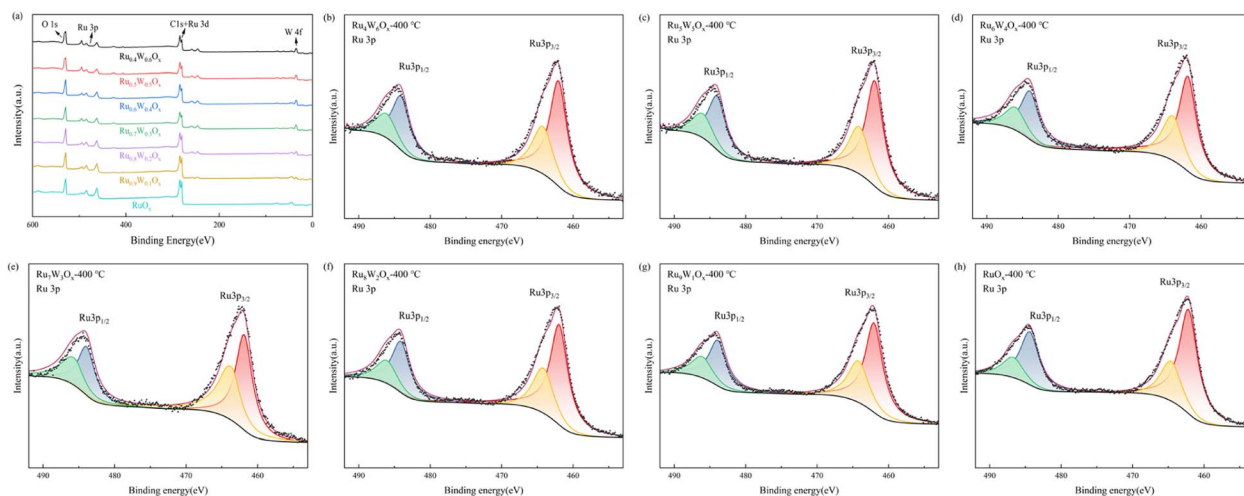
Fig. 3 XPS full spectra and Ru 3p spectra of (Ru−W)O$_x$ catalysts (a) XPS full spectra, (b) Ru$_4$W$_6$O$_x$-400 °C, (c) Ru$_5$W$_5$O$_x$-400 °C, (d) Ru$_6$W$_4$O$_x$-400 °C, (e) Ru$_7$W$_3$O$_x$-400 °C, (f) Ru$_8$W$_2$O$_x$-400 °C, (g) Ru$_9$W$_1$O$_x$-400 °C, (h) RuO$_x$-400 °C.

Table 2 The binding energy of Ru 3p peaks

Catalyst	Binding energy (eV)			
	Ru $3p_{3/2}$	Ru $3p_{3/2}$ sat.	Ru $3p_{1/2}$	Ru $3p_{1/2}$ sat.
RuO_x-400 °C	462.17	464.61	484.4	486.73
$Ru_9W_1O_x$-400 °C	462.03	464.22	483.9	486.12
$Ru_8W_2O_x$-400 °C	461.95	464.18	484.1	486.08
$Ru_7W_3O_x$-400 °C	461.90	463.7	483.91	485.64
$Ru_6W_4O_x$-400 °C	461.86	463.99	483.97	486.01
$Ru_5W_5O_x$-400 °C	461.93	464.12	483.99	486.02
$Ru_4W_6O_x$-400 °C	462.06	464.39	484.14	486.29

associated with a lower oxidation state.[32] With the W doping ratio increasing, the binding energy first decreased and then increased, with $Ru_6W_4O_x$ exhibiting the lowest binding energy. This indicates the lower Ru oxidation state and higher electron cloud density of $Ru_6W_4O_x$, which benefit the adsorption of reactants and electron transfer on the catalyst surface, accelerating the catalytic reaction, thereby enhancing catalytic performance. The trend of Ru 3p binding energy (lowest in $Ru_6W_4O_x$) is consistent with the OER activity trend (lowest overpotential in

$Ru_6W_4O_x$, Fig. 6a) and charge transfer resistance (lowest in $Ru_6W_4O_x$, Fig. 6c).

The W 4f spectra (Fig. 4 and Table 3) can be deconvoluted into two pairs of peaks: those located at 33–34 eV, 34–35 eV, 35–36 eV, and 36–37 eV correspond to the oxidation states of W^{4+} ($W4f_{7/2}$), W^{6+} (W $4f_{7/2}$), W^{4+} ($W4f_{5/2}$), and W^{6+} (W $4f_{7/2}$), respectively. Notably, the XPS W 4f spectra of $Ru_7W_3O_x$-400 °C, $Ru_6W_4O_x$-400 °C and $Ru_5W_5O_x$-400 °C show higher fractions of W^{4+}. This indicates that these catalysts contain more structural defects,[33] which facilitate electron transfer. Additionally, the binding energies of the W peak for $Ru_7W_3O_x$-400 °C and $Ru_6W_4O_x$-400 °C are relatively higher, suggesting the electron transfer from W to Ru through Ru–O–W interfacial bonds.[32,34]

The O 1s spectra (Fig. 5 and Table 4) shows a peak at approximately 531–532 eV, corresponding to surface hydroxyl groups (O_{OH}). Among the catalysts, RuO_x exhibits the lowest –OH proportion at just 9.25%, whereas the (Ru–W)O_x mixed catalysts show a significant increase in –OH content. In particular, $Ru_7W_3O_x$-400 °C and $Ru_6W_4O_x$-400 °C exhibit –OH proportions of 43.72% and 40.54%, respectively, indicating a higher prevalence of surface hydroxyl groups on these mixed catalysts. The binding energy at approximately 530 eV
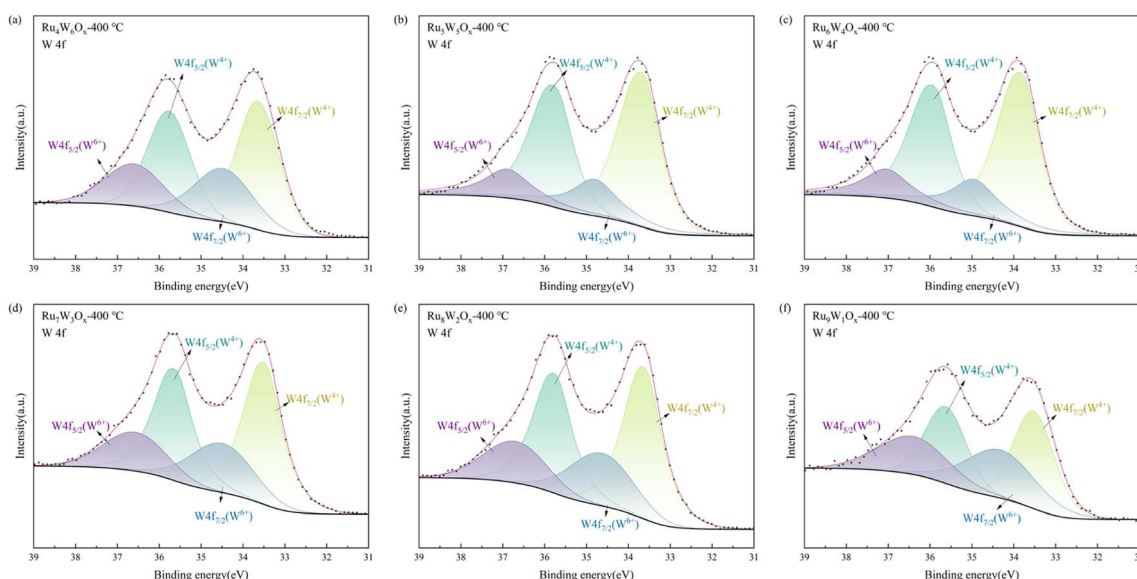

Fig. 4 W 4f XPS spectra of (Ru–W)O_x catalysts (a) $Ru_4W_6O_x$-400 °C, (b) $Ru_5W_5O_x$-400 °C, (c) $Ru_6W_4O_x$-400 °C, (d) $Ru_7W_3O_x$-400 °C, (e) $Ru_8W_2O_x$-400 °C, (f) $Ru_9W_1O_x$-400 °C.

Table 3 The binding energy and proportion of W 4f peaks

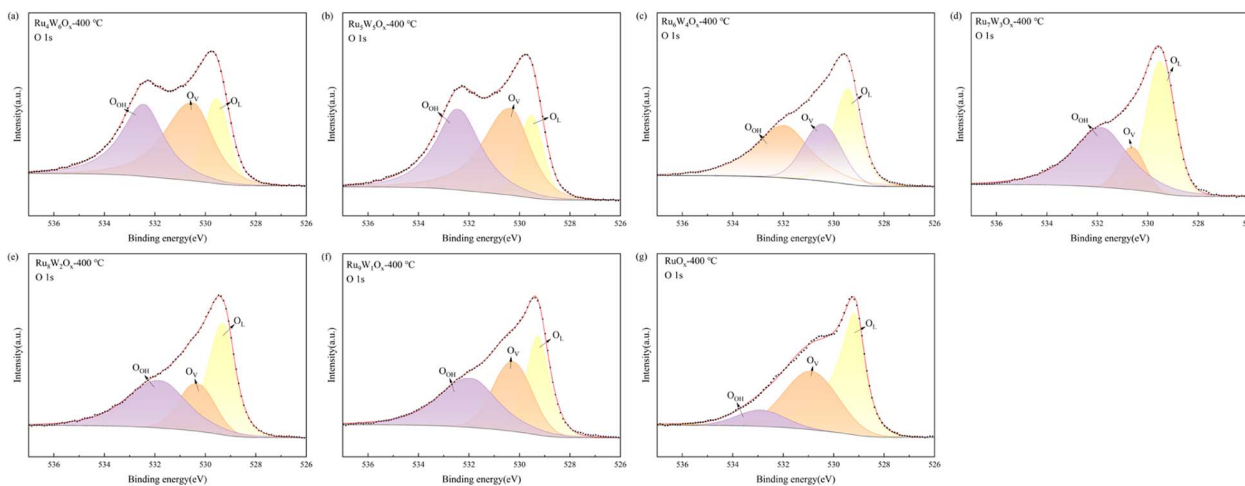| Catalysts	W $4f_{7/2}$ (W^{4+})		W $4f_{5/2}$ (W^{4+})		W $4f_{7/2}$ (W^{6+})		W $4f_{5/2}$ (W^{6+})	
	Binding energy (eV)	Proportion (%)	Binding energy (eV)	Proportion (%)	Binding energy (eV)	Proportion (%)	Binding energy (eV)	Proportion (%)
$Ru_9W_1O_x$-400 °C	33.52	27.13	35.63	27.16	34.33	22.84	36.40	22.86
$Ru_8W_2O_x$-400 °C	33.62	33.04	35.76	33.08	34.62	16.93	36.69	16.95
$Ru_7W_3O_x$-400 °C	33.74	35.36	35.87	35.40	34.66	14.61	36.76	14.62
$Ru_6W_4O_x$-400 °C	33.81	37.22	35.92	37.26	34.95	12.72	37.04	12.80
$Ru_5W_5O_x$-400 °C	33.75	35.37	35.87	34.39	34.53	15.11	36.60	15.13
$Ru_4W_6O_x$-400 °C	33.64	31.85	35.77	31.88	34.48	18.12	36.60	18.14

Fig. 5 O 1s XPS spectra of (Ru–W)O$_x$ catalysts (a) Ru$_4$W$_6$O$_x$-400 °C, (b) Ru$_5$W$_5$O$_x$-400 °C, (c) Ru$_6$W$_4$O$_x$-400 °C, (d) Ru$_7$W$_3$O$_x$-400 °C, (e) Ru$_8$W$_2$O$_x$-400 °C, (f) Ru$_9$W$_1$O$_x$-400 °C, (g) RuO$_x$-400 °C.

Table 4 The binding energy and proportion of O 1s peaks

	O$_{OH}$		O$_V$		O$_L$	
Catalysts	Binding energy (eV)	Proportion (%)	Binding energy (eV)	Proportion (%)	Binding energy (eV)	Proportion (%)
RuO$_x$-400 °C	532.88	9.25	530.89	38.93	529.16	51.83
Ru$_9$W$_1$O$_x$-400 °C	531.90	37.23	530.27	32.06	529.27	30.72
Ru$_8$W$_2$O$_x$-400 °C	531.76	38.07	530.31	21.56	529.26	40.37
Ru$_7$W$_3$O$_x$-400 °C	531.83	43.72	530.63	13.23	529.50	43.05
Ru$_6$W$_4$O$_x$-400 °C	531.96	40.54	530.44	26.96	529.41	32.50
Ru$_5$W$_5$O$_x$-400 °C	532.42	38.88	530.35	42.17	529.53	18.96
Ru$_4$W$_6$O$_x$-400 °C	532.44	36.22	530.48	41.84	529.56	21.94

corresponds to oxygen vacancies (O$_V$) within the catalyst structure, while the binding energy near 529 eV is attributed to lattice oxygen (O$_L$), typically indicative of metal oxide structures. A high proportion of lattice oxygen suggests the presence of more metal oxide structures in the catalyst. In the OER process, surface hydroxyl (O$_{OH}$) groups often serve as critical active sites, as they promote the dissociation of water molecules and facilitate oxygen formation.[8] These results highlight the enhanced surface properties and catalytic activity of Ru$_7$W$_3$O$_x$-400 °C and Ru$_6$W$_4$O$_x$-400 °C for the OER.

3.2 OER performance

The iR-corrected (90% compensation) LSV curves (Fig. 6a) demonstrate that all the synthesized (Ru–W)O$_x$ catalysts exhibit superior OER performance compared to COM-RuO$_2$. At the same current density, the overpotential of (Ru–W)O$_x$ catalysts is significantly lower than that of COM-RuO$_2$ (187.59 mV@10 mA cm^{-2} and 406.57 mV@100 mA cm^{-2}). As the W content increases, the overpotential of (Ru–W)O$_x$ catalysts initially decreases and then increases, reaching the lowest values with Ru$_6$W$_4$O$_x$ (140.32 mV@10 mA cm^{-2} and 213.16 mV@100 mA cm^{-2}), which are much lower than those of COM-RuO$_2$. This suggests that the appropriate W doping ratio can effectively

enhance the catalytic activity of the OER. However, when the W content exceeds 60 at%, the overpotential sharply increases, likely due to excessive W partially substituting or covering Ru active sites, leading to unfavorable changes in the crystal structure. The oxidation peak observed at approximately 1.65 V for COM-RuO$_2$ can be attributed to the oxidation of residual low-valence Ru species in the commercial catalyst. Due to the limited amount of oxidizable Ru^{3+}, when these low-valent Ru species are fully oxidized, the current contribution of the reaction reaches saturation, manifested as the current density no longer increases with voltage.

The Tafel slopes of Ru$_6$W$_4$O$_x$-400 °C, Ru$_7$W$_3$O$_x$-400 °C, and Ru$_5$W$_5$O$_x$-400 °C are the lowest among all catalysts, at 51.39 mV dec^{-1}, 52.02 mV dec^{-1}, and 53.47 mV dec^{-1}, respectively (Fig. 6b). This indicates that these catalysts exhibit the fastest reaction kinetics, allowing high current density at lower overpotential and making the OER process more efficient. The optimal W doping level (30–50 at%) improves the electronic structure and reaction kinetics, significantly enhancing the OER performance of Ru-based catalysts. In contrast, COM-RuO$_2$ shows the highest Tafel slope (133.93 mV dec^{-1}), reflecting the poorest OER performance and underscoring the advantages of W-doped catalysts in OER reactions.
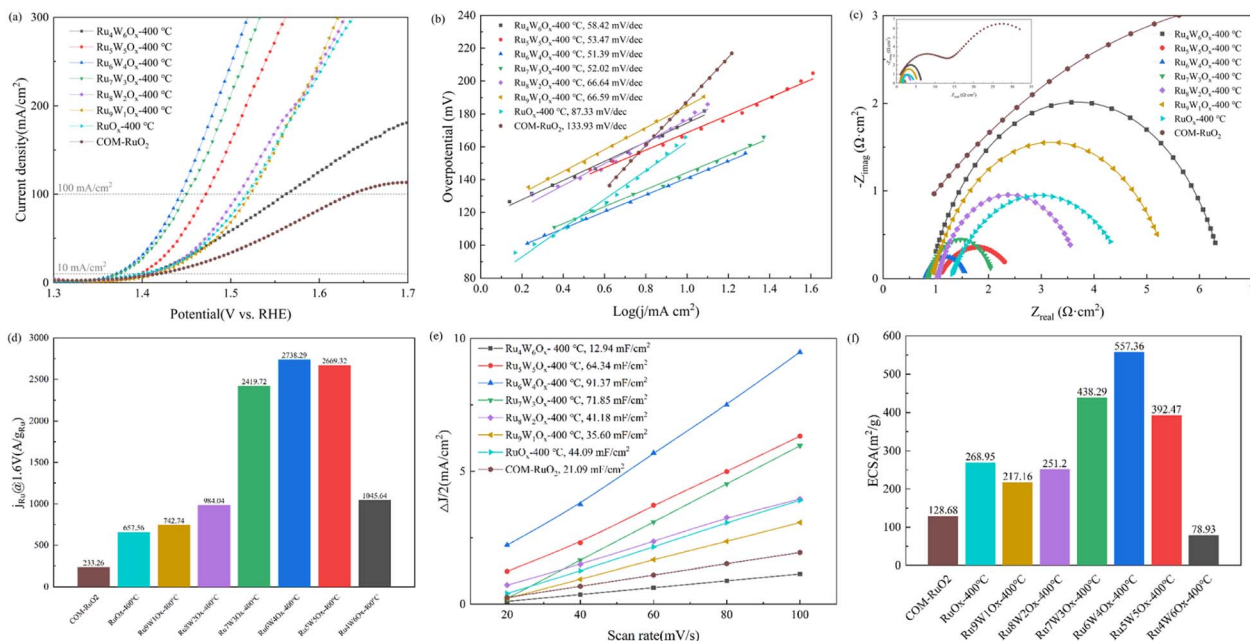
Fig. 6 OER performance of catalysts in 0.5 M H_2SO_4 (a) polarization curves of catalysts in 0.5 M H_2SO_4 (90% IR correction), (b) fitted Tafel plots of catalysts, (c) EIS diagrams of catalysts under 1.45 V (Nyquist plots), (d) mass activity of catalysts, (e) C_{dl} plots derived from CV curves, (f) ECSA's calculation results.
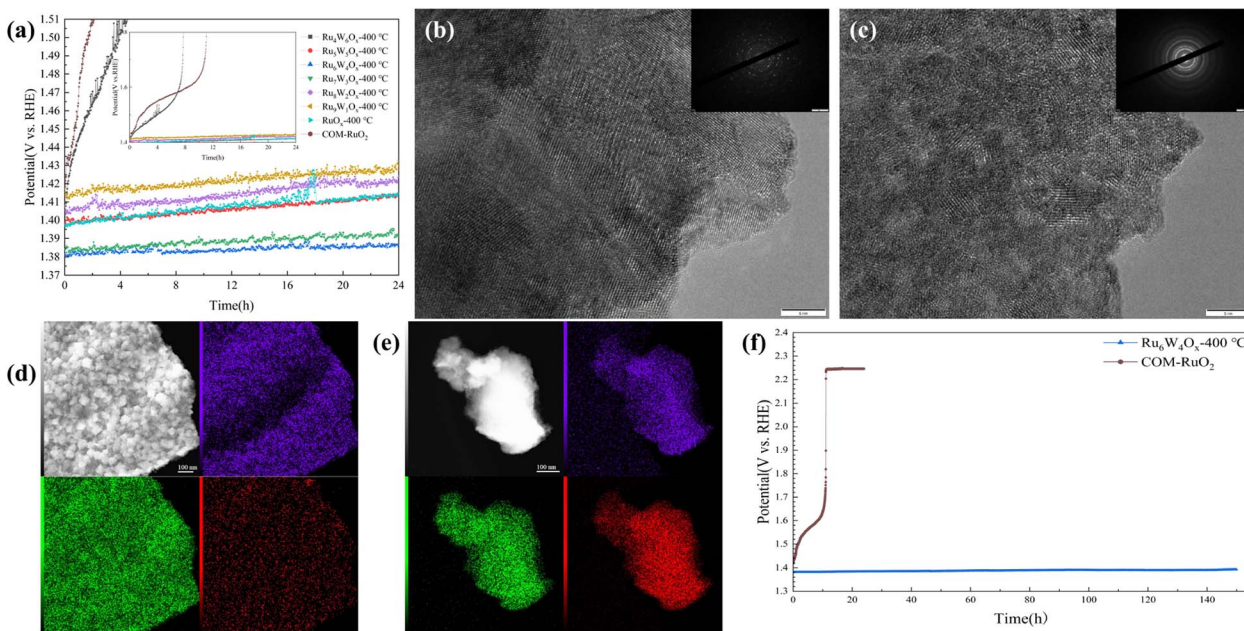

Fig. 7 Chronopotentiogram and characterization after acidic OER (a) chronopotentiogram of different catalysts at 10 mA cm^{-2}, (b) HRTEM images and SAED patterns of $Ru_4W_6O_x$-400 °C after OER, (c) HRTEM images and SAED patterns of $Ru_6W_4O_x$-400 °C after OER, (d) EDX elemental mapping of $Ru_4W_6O_x$-400 °C after OER, (e) EDX elemental mapping of $Ru_6W_4O_x$-400 °C after OER, (f) chronopotentiogram of $Ru_6W_4O_x$-400 °C and COM-RuO_2 over an extended duration.

The Nyquist plots (Fig. 6c) show the impedance characteristics of $(Ru-W)O_x$ catalysts with different doping ratios compared to COM-RuO_2. The Nyquist plot of COM-RuO_2 displays two semicircles, indicating two main limiting steps in the OER: a high-frequency process associated with charge transfer and a low-frequency process related to diffusion or

interfacial resistance. These results suggest that the catalytic performance of COM-RuO_2 is limited by its high charge transfer resistance and poor gas or ion transport properties. $Ru_4W_6O_x$-400 °C exhibits the highest charge transfer resistance, likely due to the excessive W doping reducing the electrical conductivity of the catalyst and hindering electron transfer. In contrast,

Ru$_6$W$_4$O$_x$-400 °C and Ru$_7$W$_3$O$_x$-400 °C show much higher charge transfer efficiency, with optimal W doping minimizing activation polarization and improving electron conductivity. This optimization of the electronic structure contributes to enhanced OER performance.

As shown in Fig. 6d, Ru$_6$W$_4$O$_x$-400 °C exhibits an outstanding mass activity of 2738.29 A g$_{Ru}^{-1}$ at 1.6 V, which is 4 times that of RuO$_x$ (657.56 A g$_{Ru}^{-1}$) and 12 times that of COM-RuO$_2$ (233.26 A g$_{Ru}^{-1}$).

The electrochemical double-layer capacitance (C_{dl}) was tested to calculate the ECSA (Fig. 6e and f). Ru$_6$W$_4$O$_x$-400 °C exhibited the largest ECSA of 557.36 m^2 g^{-1}, which is 2.07 times that of RuO$_x$ and 4.33 times that of COM-RuO$_2$. This indicates that Ru$_6$W$_4$O$_x$-400 °C provides the highest number of active sites for OER reactant adsorption, further validating its superior catalytic activity. The low ECSA of COM-RuO$_2$ leads to the difficulty of OER reactant adsorption and rapid desorption of O$_2$

on the surface, further inhibiting current growth, which also accounts for the phenomenon of current stagnation.

From a practical application perspective, stability in acidic media is a critical parameter for evaluating OER electrocatalysts. The chronoamperometric results (Fig. 7a) reveal the stability of various (Ru–W)O$_x$ catalysts compared to COM-RuO$_2$ during the OER. COM-RuO$_2$ shows a significant performance decline within the first hour, indicating rapid deactivation during prolonged OER reactions. Impressively, Ru$_6$W$_4$O$_x$-400 °C exhibits minimal activity decay over 24 hours, with the working electrode potential increasing by only about 3 mV. This demonstrates the high structural stability of the Ru–W doped heterostructure at this ratio. The stability enhancement is likely due to the formation of strong Ru–O–W bonds, which reduce Ru particle aggregation and dissolution. Ru particles are prone to dissolution or reconstruction under high potentials during OER. However, appropriate W doping mitigates this process,
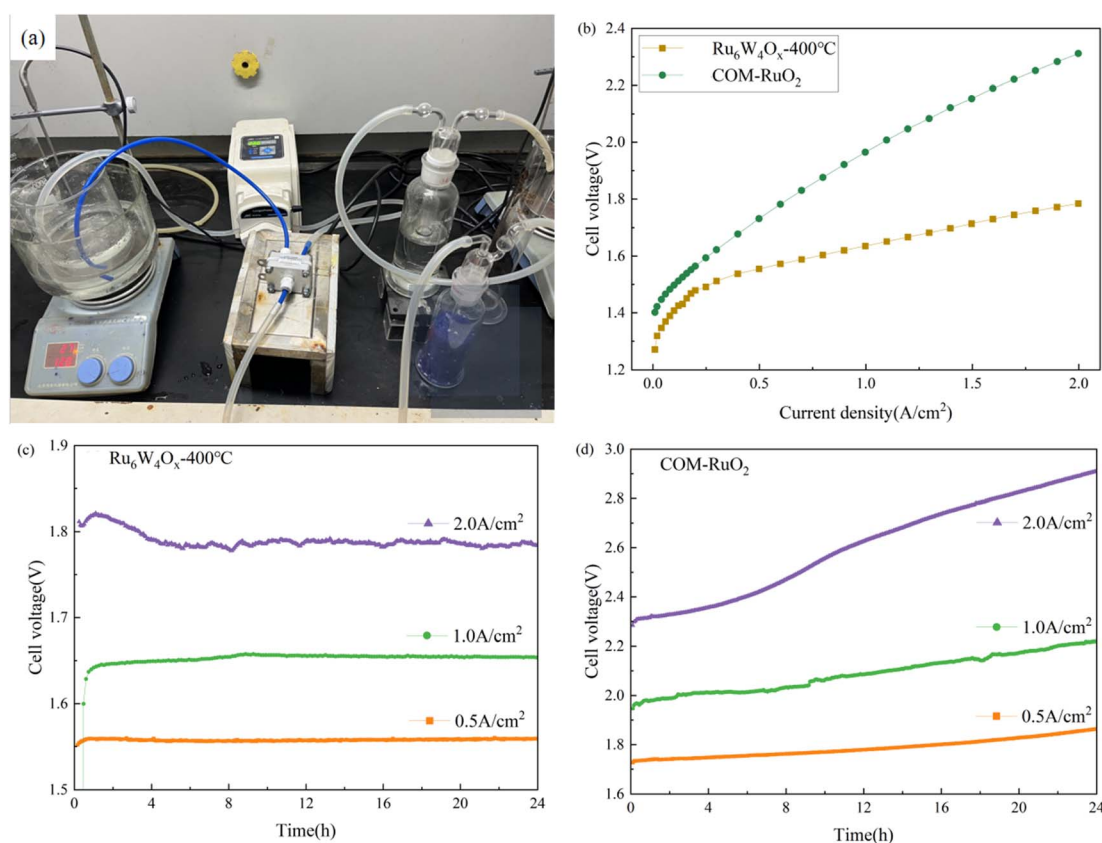

Fig. 8 PEMWE device performance at 80 °C and ambient pressure (a) photograph of the PEMWE device, (b) I−V curves of PEMWE electrolyzers using Ru$_6$W$_4$O$_x$-400 °C or COM-RuO$_2$ as anodic catalyst and commercial Pt/C as cathodic catalyst, at room temperature and ambient pressure. No cell voltages were iR compensated, (c) chronopotentiogram of Ru$_6$W$_4$O$_x$-400 °C at 0.5 A cm^{-2}, 1 A cm^{-2}, and 2 A cm^{-2}, (d) chronopotentiogram testing of COM-RuO$_2$ at 0.5 A cm^{-2}, 1 A cm^{-2}, and 2 A cm^{-2}.

Table 5 Performance of Ru$_6$W$_4$O$_x$-400 °C-based electrolyzer at 80 °C and 2 A cm^{-2}

The anode catalyst	Potential (V)	Actual H$_2$ production (L)	Theoretical H$_2$ production (L)	H$_2$ production efficiency (%)	Electrolytic efficiency (%)	Energy consumption (kWh m^{-3} H$_2$)
Ru$_6$W$_4$O$_x$-400 °C	1.784	3.288	3.343	98.34	81.72	4.34

Table 6 Comparison of representative Ru-based electrocatalysts performance

Catalyst	Electrolyte	In a three-electrode system				In a PEMWE device		Ref.
		η_{10} (mV)	Tafel slope (mV dec^{-1})	Mass activity	Stability	Voltage (V)	Stability	
Ru$_6$W$_4$O$_x$-400 °C	0.5 M H$_2$SO$_4$	140.32	51.39	2738.2 A g$_{Ru}^{-1}$@1.6 V	η_{10} increased by 3 mV in 24 h	1.784 V@2 A cm^{-2}	No decay was observed after 24 h@2 A cm^{-2}	This work
RuO$_2$ NSs	0.5 M H$_2$SO$_4$	199	38.2	0.52 A mg$_{Ru}^{-1}$@1.46 V	η_{10} increased by 32 mV in 6 h	1.65 V@0.93 A cm^{-2}	—	35
Ru$_1$-Pt$_3$Cu	0.1 M HClO$_4$	220	—	779 A g$_{Ru + Pt}^{-1}$@1.51 V	η_{10} increased by 2.1% in 28 h	—	—	16
Cu-doped RuO$_2$	0.5 M H$_2$SO$_4$	188	43.96	—	η_{10} increased by 83 mV in 8 h	—	—	30
np-UHEA12	0.5 M H$_2$SO$_4$	258	84.2	—	—	1.53 V@10 mA cm^{-2}	Voltage increased by 100 mV in 40 000 s@10 mA cm^{-2}	17
RuCu NSs/C −350 °C	0.5 M H$_2$SO$_4$	236	40.4	—	—	1.49 V@10 mA cm^{-2}	Stable for 20.5 h@5 mA cm^{-2}	18
Core–shell Ru@IrO$_x$	0.5 M H$_2$SO$_4$	282	69.1	644.8 A g$_{Ru}^{-1}$@1.56 V	Activity declined to nearly 90% in 24 h@10 mA cm^{-2}	—	—	36
RuO$_2$ NWs	0.5 M H$_2$SO$_4$	234	—	—	45 mV overpotential change in 20 h@5 mA cm^{-2}	1.50 V@10 mA cm^{-2}	Voltage increased by 30 mV in 10 h@5 mA cm^{-2}	37
Nb$_{0.1}$Ru$_{0.9}$O$_2$	0.5 M H$_2$SO$_4$	204	47.9	150.5 A g$_{Ru}^{-1}$@1.47 V	No obvious decay was observed in 300 h@200 mA cm^{-2}	1.69 V@1 A cm^{-2}	Survived for 100 h@300 mA cm^{-2}	15
Co$_{0,11}$Ru$_{0,89}$O$_{2-\delta}$ (350)	0.5 M H$_2$SO$_4$	169	49	—	η_{10} increased by 15 mV after 10 000 cycles	—	—	19
S-RuFeO$_x$	0.1 M HClO$_4$	187	40	1.18 A mg$_{Ru}^{-1}$@1.42 V	η_{10} increased by 20 mV in 10 h	—	—	20
W-IrRu$_3$O$_x$	0.5 M H$_2$SO$_4$	249	64	3.2 A mg$_{Ir+Ru}^{-1}$@1.53 V	η_{10} increased from 231 to ~300 mV in the first ~30 h	1.66 V@1 A cm^{-2} and 1.82 V@2 A cm^{-2}	Stable for 24 h@1.5 A cm^{-2}	21
Mn-RuO$_2$	0.5 M H$_2$SO$_4$	158	42.94	596.38 A g$_{Ru}^{-1}$@1.5 V	Stable for 10 h@10 mA cm^{-2}	—	—	22
Cr$_{0,6}$Ru$_{0,4}$O$_2$ (550)	0.5 M H$_2$SO$_4$	178	58	229 A g$_{Ru}^{-1}$@1.5 V	η_{10} increased by 11 mV after 10 000 cycles	—	—	23
a-RuTe$_2$ PNRs	0.5 M H$_2$SO$_4$	245 mV	—	—	—	1.52 V@10 mA cm^{-2}	Stable for 24 h@10 mA cm^{-2}	24
Ru/RuS$_2$	0.5 M H$_2$SO$_4$	201	47.2	—	Stable for 24 h@10 mA cm^{-2}	1.501 V@10 mA cm^{-2}	Slightly decayed in 10 h@ 10 mA cm^{-2}	38
Y$_2$Ru$_2$O$_{7-3}$	0.1 M HClO$_4$	190	55	—	Decreased by 0.17 mA cm^{-2} after 10 000 cycles	—	—	25

Table 6 (Contd.)

Catalyst	In a three-electrode system					In a PEMWE device		Ref.
	Electrolyte	η_{10} (mV)	Tafel slope (mV dec^{-1})	Mass activity	Stability	Voltage (V)	Stability	
M-RuO_2	0.5 M H_2SO_4	230	—	—	Stable for 4 h@1.53 V	1.9V@1 A cm^{-2}	Voltage didn't change significantly in 100 h	26
$Y_{1.7}Sr_{0.3}Ru_2O_7$	0.5 M H_2SO_4	264	44.8	1018 A g_{Ru}^{-1}@1.53 V	Stable for 28 h@10 mA cm^{-2}	—	—	27
$Nd_2Ru_2O_7$	0.1 M $HClO_4$	210	58.48	—	Stable for 6 h@1 mA cm^{-2}	—	—	28
V-$Ru_xMn_{1-x}O_2$ NWs	0.5 M H_2SO_4	200.0	48.97	—	Stable for 600 h@10 mA cm^{-2}	1.48 V@10 mA cm^{-2} &1.61 V@50 mA cm^{-2}	Stable for >30 h@500 mA cm^{-2}	29

preserving the catalyst's original nanostructure and enhancing its long-term stability. The $Ru_4W_6O_x$-400 °C, on the other hand, shows a significantly higher initial electrode potential compared to other (Ru–W)O_x catalysts due to its poor OER activity, consistent with the LSV and EIS results. Its electrode potential sharply increases after just 0.5 hours of testing, indicating rapid deactivation. This may be attributed to excessive W doping, which distorts Ru's crystal structure or forms unstable oxide phases that are prone to reconstruction or dissolution during the reaction, leading to the loss of active sites and catalyst surface passivation. The TEM images and SAED patterns of $Ru_6W_4O_x$-400 °C and $Ru_4W_6O_x$-400 °C after OER (Fig. 7b and c), demonstrate that $Ru_6W_4O_x$-400 °C maintains structural stability under OER conditions, while the structure and morphology of $Ru_4W_6O_x$-400 °C are significantly different from those before OER. According to the elemental mapping (Fig. 7d and e and Table S1), $Ru_4W_6O_x$-400 °C exhibits a significant decrease in W content, while $Ru_6W_4O_x$-400 °C shows little change.

Based on the combined OER activity and stability results, $Ru_6W_4O_x$-400 °C demonstrates a robust balance of activity and stability. Its synergistic structure and strong Ru–O–W bonds provide durable functional active sites, showcasing high potential for practical applications. Consequently, its stability was assessed over an extended duration at a constant current density of 10 mA cm^{-2} (Fig. 7f). $Ru_6W_4O_x$-400 °C demonstrated exceptional durability, exhibiting a negligible potential increase of 12 mV over 150 h of continuous operation. In contrast, COM-RuO_2 underwent rapid deactivation within 10 h.

3.3. PEMWE device performance

Finally, a PEM water electrolyzer (PEMWE) was constructed to evaluate the practical application potential of the $Ru_6W_4O_x$-400 °C catalyst for water electrolysis as shown in Fig. 8a. The electrolyzer utilized $Ru_6W_4O_x$-400 °C as the anode catalyst, commercial 60 wt% Pt/C (purchased from Suzhou Sinero Co., Ltd) as the cathode catalyst, and a proton exchange membrane (Nafion 115). Catalyst coated on membrane (CCM) is employed to prepare 2×2 cm^2 active area membrane electrode assembly (MEA). For comparison, another electrolyzer was assembled using COM-RuO_2 as the anode catalyst, with all other conditions kept identical.

The polarization curves (Fig. 8b) show that the electrolyzer using the self-synthesized $Ru_6W_4O_x$-400 °C catalyst exhibits significantly lower voltages across the entire current density range compared to the COM-RuO_2-based system. This indicates that the self-synthesized catalyst achieves lower energy consumption at the same current density.

Due to laboratory safety regulations, chronoamperometric tests were conducted at current densities of 0.5 A cm^{-2}, 1 A cm^{-2}, and 2 A cm^{-2} for 24 hours (Fig. 8c and d) to assess the stability of the catalysts. The electrochemical stability of the electrolyzers varied significantly between the self-synthesized $Ru_6W_4O_x$-400 °C catalyst and COM-RuO_2, especially at high current densities. The $Ru_6W_4O_x$-400 °C-based electrolyzer demonstrated stable voltage throughout the 24 hours test,

maintaining a consistent voltage of approximately 1.78 V at 2 A cm^{-2} with minimal fluctuations, indicating excellent stability. In contrast, the COM-RuO$_2$-based electrolyzer exhibited significantly poorer electrochemical stability under the same conditions. At 2 A cm^{-2}, its initial voltage of 2.2 V increased to nearly 2.8 V over the 24 hours test, showing a clear trend of voltage degradation.

Additionally, hydrogen production efficiency, electrolysis efficiency, and energy consumption values for Ru$_6$W$_4$O$_x$-400 °C at a current density of 2 A cm^{-2} and a working temperature of 80 °C were calculated and are presented in Table 5. The electrolyzer with Ru$_6$W$_4$O$_x$-400 °C as the anode catalyst achieved a lower cell voltage of 1.784 V and hydrogen production energy consumption of 4.34 kWh m^{-3} H$_2$, with an electrolysis efficiency of 81.72%.

Representative Ru-based catalysts for PEM electrolyzer were systematically compared in Table 6. The Ru$_6$W$_4$O$_x$-400 °C catalyst developed in this work demonstrates significant advantages, including a remarkably low overpotential of 140.32 mV@10 mA cm^{-2}, an ultrahigh mass activity of 2738.2 A g$_{Ru}$$^{-1}$ at 1.6 V, exceptional stability with only a 3 mV increase in η_{10} over 24 hours. Notably, it achieves a competitive operating voltage of 1.784 V at 2 A cm^{-2}, and maintains no performance decay after 24 hours under practical high-current-density conditions. These metrics collectively highlight its potential for efficient water electrolysis systems.

4 Conclusion

A cost-effective anode catalyst for hydrogen production *via* PEM water electrolysis was developed using a co-doping strategy with Ru and W. The incorporation of tungsten not only reduces the reliance on expensive noble metals but also improves the catalyst's activity and stability through its synergistic interaction with ruthenium. Using a simple and efficient preparation process, tungsten was introduced at an optimal ratio, which increased the number of active sites and facilitated precise control over the catalyst's nanoscale structure, significantly enhancing its electrochemical performance for the oxygen evolution reaction. The optimized Ru$_6$W$_4$O$_x$-400 °C catalyst demonstrated remarkable catalytic efficiency and durability, achieving an overpotential of just 140.32 mV at 10 mA cm^{-2} with only a 12 mV in overpotential increase after 150 hours of continuous electrolysis. Additionally, a PEMWE employing Ru$_6$W$_4$O$_x$-400 °C as the anode catalyst delivered outstanding performance, achieving a cell voltage as low as 1.784 V at a current density of 2 A cm^{-2}, an energy consumption of 4.34 kWh m^{-3} H$_2$, and an electrolysis efficiency of 81.72%. As summarized in Table 6, the Ru$_6$W$_4$O$_x$-400 °C catalyst exhibits clear advantages over other catalysts. This work contributes to advancing the development of low-cost, high-efficiency water electrolysis technology for hydrogen production.

Conflicts of interest

There are no conflicts to declare.

Data availability

The data that supports the findings of this study are available from the corresponding authors upon reasonable request.

Supplementary information: experimental details, supplementary tables and the effect of annealing temperature on catalyst performance. See DOI: https://doi.org/10.1039/d5ra05145b.

References

1 M. Younas, S. Shafique, A. Hafeez, F. Javed and F. Rehman, *Fuel*, 2022, **316**, 123317.
2 M. El-Shafie, *Results Eng.*, 2023, 20.
3 S. Shiva Kumar and H. Lim, *Sustainable Energy Fuels*, 2023, 7, 3560–3583.
4 S. M. Kang, Z. H. Pan, J. J. Guo, Y. X. Zhou, J. Y. Wang, L. D. Fan, C. H. Zheng, S. W. Cha and Z. Zhong, *Front. Energy*, 2024, **18**, 583–611.
5 M. Nasser, T. F. Megahed, S. Ookawara and H. Hassan, *Environ. Sci. Pollut. Res. Int.*, 2022, **29**, 86994–87018.
6 G. B. Jung, S. H. Chan, C. J. Lai, C. C. Yeh and J. W. Yu, *Energies*, 2019, **12**, 4218.
7 S. Zhang, X. Ma, Y. He, Y. Zhu and Z. Wang, *Int. J. Hydrogen Energy*, 2023, **48**, 10532–10544.
8 Y. Wen, P. Chen, L. Wang, S. Li, Z. Wang, J. Abed, X. Mao, Y. Min, C. T. Dinh and P. D. Luna, *J. Am. Chem. Soc.*, 2021, **143**, 6482–6490.
9 X. Ma, L. Deng, M. Lu, Y. He, S. Zou and Y. Xin, *Nanotechnology*, 2022, **33**, 125702.
10 Y. P. Liu, X. Liang, H. Chen, R. Q. Gao, L. Shi, L. Yang and X. X. Zou, *Chin. J. Catal.*, 2021, **42**, 1054–1077.
11 K. Perovi, S. Morovi, A. Juki and K. Kouti, *Materials*, 2023, **16**, 6319.
12 Y. Cheng, Y. Wang, Z. Shi, H. Wu, J. Yang, J. Ni, M. Yang, Z. Wang, M. Xiao, C. Liu and W. Xing, *EcoEnergy*, 2025, **3**, 131–155.
13 Y. Wang, H. Pan, Z. Liu and P. Kang, *Trans. Tianjin Univ.*, 2024, **30**, 395–405.
14 Z. W. Lei, T. Y. Wang, B. T. Zhao, W. B. Cai, Y. Liu, S. H. Jiao, Q. Li, R. G. Cao and M. L. Liu, *Adv. Energy Mater.*, 2020, **10**, 2000478.
15 H. Liu, Z. Zhang, J. Fang, M. Li, M. G. Sendeku, X. Wang, H. Wu, Y. Li, J. Ge, Z. Zhuang, D. Zhou, Y. Kuang and X. Sun, *Joule*, 2023, **7**, 558–573.
16 Y. Yao, *Engineering the Electronic Structure of Single Atom Ru Sites via Compressive Strain Boosts Acidic Water Oxidation Electrocatalysis*, Springer, 2022.
17 Z. X. Cai, H. Goou, Y. Ito, T. Tokunaga, M. Miyauchi, H. Abe and T. Fujita, *Chem. Sci.*, 2021, **12**, 11306–11315.

18 Q. Yao, B. Huang, N. Zhang, M. Sun, Q. Shao and X. Huang, *Angew. Chem.*, 2019, **131**, 14121–14126.

19 Y. Tian, S. Wang, E. Velasco, Y. Yang, L. Cao, L. Zhang, X. Li, Y. Lin, Q. Zhang and L. Chen, *iScience*, 2020, **23**, 100756.

20 Y. Xue, J. Fang, X. Wang, Z. Xu, Y. Zhang, Q. Lv, M. Liu, W. Zhu and Z. Zhuang, *Adv. Funct. Mater.*, 2021, **31**, 2101405.

21 S. Wang, J. Zang, W. Shi, D. Zhou, Y. Jia, J. Wu, W. Yan, B. Zhang, L. Sun and K. Fan, *ACS Appl. Mater. Interfaces*, 2023, **15**, 59432–59443.

22 S. Chen, H. Huang, P. Jiang, K. Yang, J. Diao, S. Gong, S. Liu, M. Huang, H. Wang and Q. Chen, *ACS Catal.*, 2019, **10**, 1152–1160.

23 Y. Lin, Z. Tian, L. Zhang, J. Ma, Z. Jiang, B. J. Deibert, R. Ge and L. Chen, *Nat. Commun.*, 2019, **10**, 162.

24 J. Wang, L. Han, B. Huang, Q. Shao, H. L. Xin and X. Huang, *Nat. Commun.*, 2019, **10**, 5692.

25 J. Kim, P. C. Shih, K. C. Tsao, Y. T. Pan, X. Yin, C. J. Sun and H. Yang, *J. Am. Chem. Soc.*, 2017, **139**, 12076–12083.

26 G. Zhao, W. Guo, M. Shan, Y. Fang, G. Wang, M. Gao, Y. Liu, H. Pan and W. Sun, *Adv. Mater.*, 2024, **36**, 2404213.

27 N. Zhang, C. Wang, J. Chen, C. Hu, J. Ma, X. Deng, B. Qiu, L. Cai, Y. Xiong and Y. Chai, *ACS Nano*, 2021, **15**, 8537–8548.

28 H. Liu, Z. L. Wang, M. X. Li, X. P. Zhao, X. X. Duan, S. Y. Wang, G. Y. Tan, Y. Kuang and X. M. Sun, *Sci. China Mater.*, 2021, **64**, 1653–1661.

29 H. Zhu, Y. J. Wang, Z. Q. Jiang, B. L. Deng and Z. J. Jiang, *J. Mater. Chem. A*, 2023, **11**, 25252–25261.

30 J. Su, R. Ge, K. Jiang, Y. Dong, F. Hao, Z. Tian, G. Chen and L. Chen, *Adv. Mater.*, 2018, **30**, 1801351.

31 C. V. Pham, D. Escalera-López, K. Mayrhofer, S. Cherevko and S. Thiele, *Adv. Energy Mater.*, 2021, **11**, 2101998.

32 X. F. Wang, H. Jang, S. G. Liu, Z. J. Li, X. H. Zhao, Y. F. Chen, M. G. Kim, Q. Qin and X. Liu, *Adv. Energy Mater.*, 2023, **13**, 2301673.

33 X. H. Tan, W. Y. Gou, L. Q. Liao, Y. Y. Ma and Y. Q. Qu, *Mater. Chem. Front.*, 2023, **7**, 4984–4992.

34 K. Zhou, H. Liu, Z. Liu, X. Li, N. Wang, M. Wang, T. Xue, Y. Shen, H. Li, H. Li and C. Li, *Angew. Chem.*, 2025, **64**, e202422707.

35 Z. L. Zhao, Q. Wang, X. Huang, Q. Feng, S. Gu, Z. Zhang, H. Xu, L. Zeng, M. Gu and H. Li, *Energy Environ. Sci.*, 2020, **13**, 5143–5151.

36 J. Q. Shan, C. X. Guo, Y. H. Zhu, S. M. Chen, L. Song, M. Jaroniec, Y. Zheng and S. Z. Qiao, *Chem*, 2019, **5**, 445–459.

37 J. Yang, Y. Ji, Q. Shao, N. Zhang, Y. Li and X. Huang, *Adv. Funct. Mater.*, 2018, **28**, 1803722.

38 J. Zhu, Y. Guo, F. Liu, H. Xu, L. Gong, W. Shi, D. Chen, P. Wang, Y. Yang, C. Zhang, J. Wu, J. Luo and S. Mu, *Angew Chem. Int. Ed. Engl.*, 2021, **60**, 12328–12334.